



Hydrogen Variability in the Murray Formation, Gale Crater, Mars

N. H. Thomas, B. L. Ehlmann, W. Rapin, F. Rivera-Hernández, N. T. Stein,
J. Frydenvang, T. Gabriel, P. -Y. Meslin, S. Maurice, R. C. Wiens

► To cite this version:

N. H. Thomas, B. L. Ehlmann, W. Rapin, F. Rivera-Hernández, N. T. Stein, et al.. Hydrogen Variability in the Murray Formation, Gale Crater, Mars. *Journal of Geophysical Research. Planets*, 2020, 125, 10.1029/2019JE006289 . insu-03673122

HAL Id: insu-03673122

<https://insu.hal.science/insu-03673122>

Submitted on 20 May 2022

HAL is a multi-disciplinary open access archive for the deposit and dissemination of scientific research documents, whether they are published or not. The documents may come from teaching and research institutions in France or abroad, or from public or private research centers.

L'archive ouverte pluridisciplinaire **HAL**, est destinée au dépôt et à la diffusion de documents scientifiques de niveau recherche, publiés ou non, émanant des établissements d'enseignement et de recherche français ou étrangers, des laboratoires publics ou privés.



Distributed under a Creative Commons Attribution - NonCommercial - NoDerivatives 4.0 International License

**Special Section:**

Investigations of Vera Rubin Ridge, Gale Crater

Key Points:

- Murray formation bedrock points measured by ChemCam have an interquartile range of 2.3–3.1 wt.% H₂O
- Specific intervals like the Vera Rubin ridge contain high H and indicate phases including iron oxyhydroxides, akageneite, and jarosite
- Variations in water content indicate changes in depositional lake water chemistry and multiple subsequent groundwater episodes

Correspondence to:N. H. Thomas,
nhthomas@caltech.edu**Citation:**

Thomas, N. H., Ehlmann, B. L., Rapin, W., Rivera-Hernández, F., Stein, N. T., Frydenvang, J., et al. (2020). Hydrogen variability in the Murray formation, Gale crater, Mars. *Journal of Geophysical Research: Planets*, 125, e2019JE006289. <https://doi.org/10.1029/2019JE006289>

Received 22 NOV 2019

Accepted 9 MAR 2020

Accepted article online 20 APR 2020

Hydrogen Variability in the Murray Formation, Gale Crater, Mars

N. H. Thomas¹ , B. L. Ehlmann^{1,2} , W. Rapin¹ , F. Rivera-Hernández³ , N. T. Stein¹ , J. Frydenvang⁴ , T. Gabriel⁵ , P.-Y. Meslin⁶ , S. Maurice⁶, and R. C. Wiens⁷

¹Division of Geological and Planetary Sciences, California Institute of Technology, Pasadena, CA, USA, ²Jet Propulsion Laboratory, California Institute of Technology, Pasadena, CA, USA, ³Earth Sciences, Dartmouth College, Hanover, NH, USA, ⁴Natural History Museum, University of Copenhagen, Copenhagen, Denmark, ⁵School of Earth and Space Exploration, Arizona State University, Tempe, AZ, USA, ⁶Institut de Recherche en Astrophysique et Planétologie, Université de Toulouse, CNRS, UPS, CNES, Toulouse, France, ⁷Los Alamos National Laboratory, Los Alamos, NM, USA

Abstract The Mars Science Laboratory (MSL) *Curiosity* rover is exploring the Murray formation, a sequence of heterolithic mudstones and sandstones recording fluvial deltaic and lake deposits that comprise over 350 m of sedimentary strata within Gale crater. We examine >4,500 Murray formation bedrock points, employing recent laboratory calibrations for ChemCam laser-induced breakdown spectroscopy H measurements at millimeter scale. Bedrock in the Murray formation has an interquartile range of 2.3–3.1 wt.% H₂O, similar to measurements using the Dynamic Albedo of Neutrons and Sample Analysis at Mars instruments. However, specific stratigraphic intervals include high H targets (6–18 wt.% H₂O) correlated with Si, Mg, Ca, Mn, or Fe, indicating units with opal, hydrated Mg sulfates, hydrated Ca sulfates, Mn-enriched units, and akageneite or other iron oxyhydroxides, respectively. One stratigraphic interval with higher hydrogen is the Sutton Island unit and Blunts Point unit contact, where higher hydrogen is associated with Fe-rich, Ca-rich, and Mg-rich points. A second interval with higher hydrogen occurs in the Vera Rubin ridge portion of the Murray formation, where higher hydrogen is associated with Fe-rich, Ca-rich, and Si-rich points. We also observe trends in the H signal with grain size, separate from chemical variation, whereby coarser-grained rocks have higher hydrogen. Variability in the hydrogen content of rocks points to a history of water-rock interaction at Gale crater that included changes in lake water chemistry during Murray formation deposition and multiple subsequent groundwater episodes.

Plain Language Summary We measured the water content of bedrock targets in the Murray formation, a sequence of mudstones and sandstones part of Gale crater's Mt. Sharp, by applying recent laboratory calibrations to measurements from the *Curiosity* ChemCam instrument. While most rocks contained 2.3–3.1 wt.% H₂O, consistent with measurements by other Mars Science Laboratory instruments, we found some stratigraphic intervals contained high water content (6–18 wt.% H₂O) rocks including the Vera Rubin ridge. Based on our analysis of the corresponding major element composition, these are likely clays, Ca sulfates, Mn-enriched units, and akageneite or other iron oxyhydroxides. The variation in water content indicates a history of water-rock interaction at Gale crater that included changes in lake water chemistry during Murray formation deposition and multiple subsequent groundwater episodes.

1. Introduction

The Mars Science Laboratory (MSL) *Curiosity* rover is investigating the sedimentary stratigraphy of Gale crater's Mt. Sharp, which formed ~3.8–3.6 Ga ago and contains a sequence of clay-, hematite-, silica-, and sulfate-bearing units identified from orbit (Fraeman et al., 2016; Milliken et al., 2010). Mt. Sharp's lowermost strata are composed of fine-grained, laminated mudstones, as well as heterolithic mudstones and sandstones, which are interpreted to record mainly fluvial deltaic and lake deposits (Grotzinger et al., 2015; Hurowitz et al., 2017; Rapin et al., 2019) and are collectively called the Murray formation; these are the focus of our study. Prior work has reported variation in the chemical index of alteration (CIA; Mangold et al., 2019), mineralogy (Rapine et al., 2017), and the crystal chemistry of clay minerals as the rover traversed the Murray formation (Bristow et al., 2018). Changes in bulk hydrogen present as water or OH in basaltic sedimentary materials and specific hydrated phases aid the determination of the

degree of water-rock interaction, the style of aqueous alteration of rock units, and markers of past environments.

Curiosity measures the H content of samples with four instruments: Dynamic Albedo of Neutrons (DAN), Sample Analysis at Mars (SAM), CheMin, and ChemCam. The DAN instrument assesses hydrogen content at depths of ~45–70 cm and with a lateral footprint of ~80 cm (full width at half maximum) (Mitrofanov et al., 2012). In the Murray formation, passive DAN measurements showed an average water content of 1.7 ± 0.7 wt.% H₂O for the rocks traversed between Sols 753 and 1292 (Tate et al., 2019). The SAM instrument detects H₂O and H₂ released from drilled, particulate samples upon pyrolysis (Mahaffy et al., 2012) and measured 1.1 ± 0.6 to 2.3 ± 1.5 wt% H₂O for the first four Murray formation rock samples (Buckskin, Telegraph Peak, Mojave, and Confidence Hills) measured by *Curiosity* (Sutter et al., 2017). CheMin is also capable of identifying crystalline minerals that host hydrogen in their structure (Blake et al., 2012) and has quantified jarosite, gypsum, bassanite, opal, and phyllosilicate abundances (e.g., Rampe et al., 2017) including clay mineral abundances up to ~28 wt.% (Bristow et al., 2018).

The ChemCam instrument, which uses Laser-Induced Breakdown Spectroscopy (LIBS), can characterize sample geochemistry and hydrogen content at submillimeter scale. It has a large data set with >23,000 locations measured to date. ChemCam has been previously used to detect hydrogen in soils and rocks in Gale crater (e.g., Meslin et al., 2013; Schröder et al., 2015) with increasingly quantitative work. After the initial detection of H in calcium sulfate (Nachon et al., 2014; Schröder et al., 2015), ChemCam determined the presence of bassanite in most mineralized veins (Rapin et al., 2016), opal at Marias Pass and Naukluft Plateau (Rapin et al., 2018), and hydrated Mg sulfates at Sutton Island (Rapin et al., 2019).

Here, we applied the recent improved laboratory calibrations of H by Rapin, Meslin, et al. (2017) and Thomas et al. (2018) to quantify the bulk H content of the entire Murray formation bedrock measured to date with ChemCam. We searched for quantitative trends in bulk rock H with stratigraphic level, formation member, and rock grain size. We examined the relationship to units identified from orbit and detected with other instruments. We also cataloged the specific instances of H-enriched areas and identified the high-H phases present that indicate changes in depositional environment or style of diagenesis.

2. Methods

The ChemCam instrument measures the elemental composition of fine-scale (350–550 μm diameter) points <7 m from the rover (Maurice et al., 2012; Wiens et al., 2012). Major element compositions are calculated for all points using multivariate analysis techniques (Anderson et al., 2017; Clegg et al., 2017). Volatile elements like H are detectable but difficult to quantify by multivariate analysis given very few or only weak (e.g., Rapin, Bousquet, et al., 2017; Thomas et al., 2018). We apply standard ChemCam data preprocessing techniques (Wiens et al., 2013) followed by the peak fitting and normalization techniques described in detail by Thomas et al. (2018) to report the normalized H 656.5 nm peak area. We normalized by dividing by the O 778 nm peak area (Thomas et al., 2018; Rapin, Meslin, et al., 2017), a nearby emission line in the same spectrometer and detector, which has recently been shown to be relatively insensitive to sample matrix in the laboratory (Schröder et al., 2019).

ChemCam H peak area values have associated uncertainties from fitting the normalized spectra with an automated routine. In our laboratory characterization of H in basaltic materials, we measured homogeneous powdered pellets at five different point locations and found the standard deviation of the normalized (to O 778 nm) peak area was typically 0.01 (Thomas et al., 2018). In addition, we quantified the uncertainty in our ability to predict weight percent H from LIBS H peak areas by measuring the scatter from our fit to linear trends in the laboratory data. For the O 778 nm normalization and for samples with less than 1.25 wt.% H, we found uncertainties of ± 0.24 wt.% H or ± 2.1 wt.% H₂O as one-sigma standard deviation (Thomas et al., 2018). This uncertainty in predicting water content is high, but averaging the prediction for multiple (5–10) ChemCam observation points in a typical raster of a single target, assuming the H content is constant, the uncertainty decreases to ± 0.8 wt.% H₂O. This is within the uncertainty in predicting H content with LIBS estimated by Ytsma and Dyar (2018) of ± 1.5 wt.% H₂O.

To minimize the impact of physical matrix effects caused by varying surface properties, we limited our study to bedrock targets with no clear cracks or varying surface geometries, which may cause artificial

enhancement in the H signal from surface roughness (Rapin, Bousquet, et al., 2017). Spectra from the first five laser shots at each location were excluded from analysis due to potential dust and surface effects. We visually inspected accompanying colocated context Remote Micro-Imager and MastCam images to classify all ChemCam point-to-point data as soil, bedrock, float rock, or diagenetic feature (vein or nodule). Only points on bedrock were used in the following analyses.

In addition to H content, another factor potentially influencing the LIBS H signal response is the target's grain size (Rapin, 2016; Thomas et al., 2018). Consequently, for ChemCam targets up to Sol 1816, we compare our H measurements to grain sizes estimated using the Gini index mean score, a grain-size proxy that uses ChemCam LIBS data (Rivera-Hernández et al., 2019). The Gini index mean score quantifies the compositional variability between ChemCam LIBS shots for each rock target. Rocks with grains smaller than the LIBS spot size can yield bulk rock compositions and low point-to-point variability resulting in low Gini index mean scores (Rivera-Hernández et al., 2019). In contrast, rocks with grains about the size or larger than the LIBS spot size may have compositional contributions from individual grains and have higher point to point variability resulting in higher Gini index mean scores (Rivera-Hernández et al., 2019). The Gini index mean score was calibrated to grain size by quantifying the point-to-point chemical variability in Murray formation rocks with known grain size from images (Rivera-Hernández et al., 2020). Using this calibration, Gini index mean score grain size estimates are reported here as mud (GS1), coarse silt to very fine sand (GS2), very fine to medium sand (GS3), and medium to very coarse sand (GS4). The accuracy of the Gini index mean score to estimate grain size has been examined by comparison to grain size measurements from MAHLI (Mars Hand Lens Imager) images (Rivera-Hernández et al., 2019, 2020) and depends on a variety of factors, such as grain size sorting and the diversity in grain composition (Rivera-Hernández et al., 2019, 2020).

Additional potential sources of variability in estimated H content are detailed in Section 5.1.

3. Geologic Context

The Curiosity rover has ascended more than 400 m of stratigraphy of Mt. Sharp thus far, encountering strata consisting of fluvial, deltaic, lacustrine, and eolian sediments (Banham et al., 2018; Fraeman et al., 2016; Grotzinger et al., 2014, 2015; Williams et al., 2013). These strata comprise three stratigraphic groups: (1) the Bradbury group, (2) the Mt. Sharp group, and (3) the Siccar Point group.

The Bradbury group sits at the base of Mt. Sharp and consists of rocks interpreted to be lacustrine mudstones and a series of pebbly sandstones, conglomerates, and siltstone sedimentary rocks of fluvio-deltaic origin (Grotzinger et al., 2015).

The rover traverse so far through the Mt. Sharp group has been within the Murray formation, which consists of predominantly lacustrine mudstone with occasional intercalated cross-stratified prodeltaic, fluvial, or eolian sandstones (Grotzinger et al., 2015; Gwizd et al., 2019; Fedo et al., 2018; Stack et al., 2019; Rivera-Hernández et al., 2020). The Murray formation is at least 350 m thick and has been subdivided into eight members, which include, in ascending stratigraphic order, the Pahrump Hills member, Hartmann's Valley member, Karasburg member, Sutton Island member, Blunts Point member, Pettegrove Point member, Jura member, and Knockfarril Hill member (Figure 1a). The Pahrump Hills member is predominantly thinly laminated mudstone interpreted as hyperpycnal plume deposits in a freshwater lake (Grotzinger et al., 2015; Stack et al., 2019). In contrast, the Hartmann's Valley member contains decimeter- to meter-scale cross-stratified deposits indicative of eolian or possible fluvial reworking (Fedo et al., 2018; Gwizd et al., 2019). The overlying ~30 m thick Karasburg member once again contains persistent finely laminated mudstones interpreted as lacustrine. The Sutton Island member is a heterolithic mudstone-sandstone with disaggregated meter-scale blocks of bedrock and textural evidence of episodic drying including mud-cracks and sulfate enrichments (Rapin et al., 2019; Stein et al., 2018). The Blunts Point, Pettegrove Point, and Jura members consist of finely laminated mudstone interpreted to result from deposition of suspended sediment in a lacustrine environment (Fedo et al., 2018) and exhibit varying degrees of apparent structural deformation (Edgar et al., 2020). The Pettegrove Point and Jura members collectively comprise the Vera Rubin ridge, a ~6.5 km long, ~200 m wide topographic rise on the northwest flank of Mt. Sharp with spatially variable diagenetic alteration (Fraeman et al., 2013, 2016; 2020). The Knockfarril Hill member is in the clay-bearing unit, beyond VRR, and is beyond the scope of this paper.

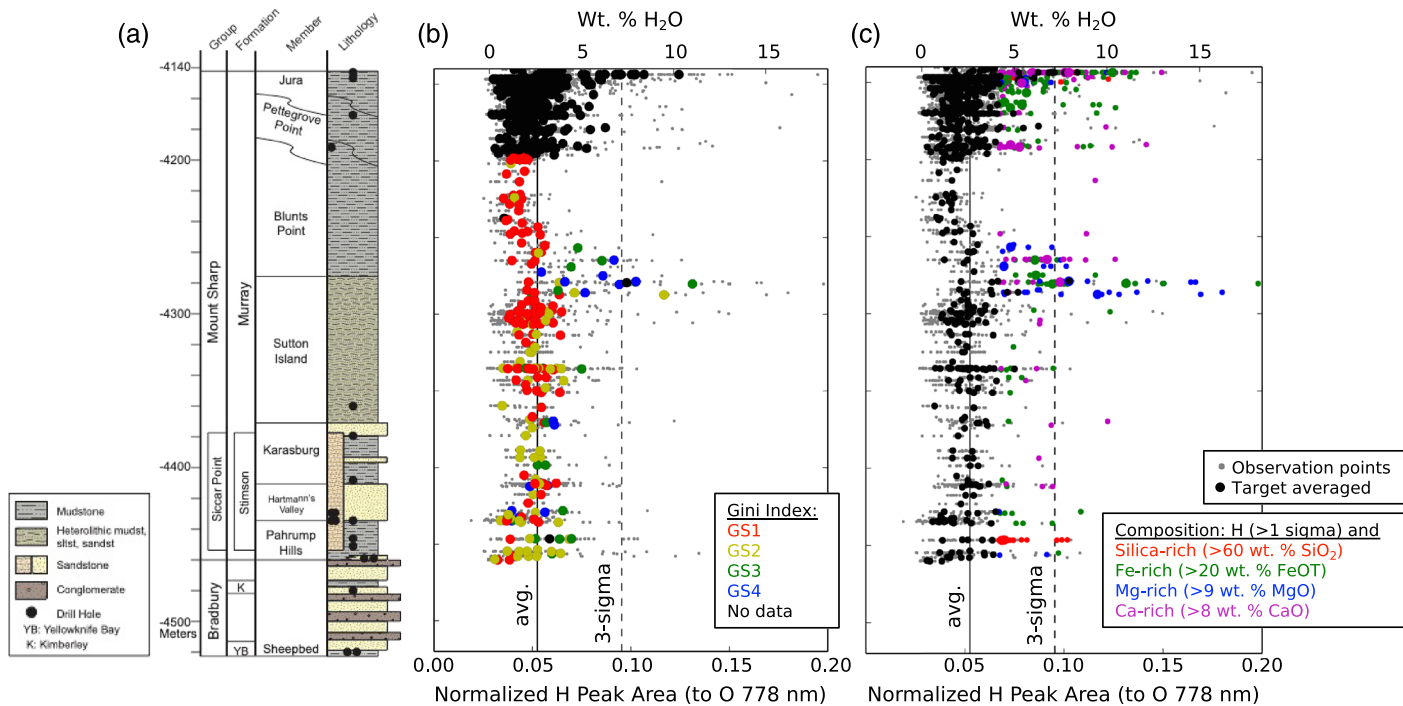


Figure 1. (a) The Gale crater stratigraphic column (Fedo et al., 2018) with drill sites marked as solid black points and (b and c) the normalized H peak area versus elevation for all ChemCam measured Murray formation bedrock targets. The smaller points are individual point observations, and the larger points are target averaged. Colors in (b) indicate Gini index mean score approximated grain size classes, when available (from Rivera-Hernández et al., 2020). Colors in (c) indicate compositions of high Si, Fe, Mg, or Ca.

The Siccar Point group unconformably overlies the Mt. Sharp group and was encountered by Curiosity along ~75 m of the Murray formation strata where it is unconformably overlain by the Stimson formation, an eolian deposit consisting of distinctive meter-scale cross-bedded sandstone (Banham et al., 2018).

4. Results

4.1. Statistics: Median Hydrogen Content and Grain Size

From Sol 766 to 2339 of the mission, 4,758 observation points, comprising 627 Murray bedrock targets, were measured by ChemCam. The observed 0.05 mean normalized H peak area (Figure 2) corresponds to 2.6 wt.% H₂O using our laboratory calibration (Thomas et al., 2018). The middle 50% of the data, that is, the interquartile range (IQR), is 0.04–0.06 (1.3–3.4 wt.% H₂O), representing the range of typical Murray formation bedrock. ChemCam observed 292 outlier points with normalized peak areas >0.08 or >5.5 wt.% H₂O, and anomalously high H signals up to 18 wt.% H₂O. Thirty-six observation points (0.7%) have no detected H content.

The mean ChemCam H signal varies significantly with some of the members of the Murray formation (Table 1). To statistically test this, we applied a Welch's *t* test using *scipy*. The assumptions of this test have been met because the ChemCam points are independent samples and the number of observation points in each group is large so the distributions are close to normal by the central limit theorem. Although large sample sizes, the distributions are skewed and do not pass normal distribution tests, so the *t* test results should be treated with caution. The Hartmann's Valley member shows lower hydrogen (mean \pm standard deviation: 1.9 ± 1.5 wt.% H₂O), in spite of the fact it is generally coarser (Figure 1), which typically correlates with higher hydrogen peaks due to roughness for the same H content (Rapin, Bousquet, et al., 2017). Most of the high H targets occur at the Sutton Island/Blunts Point transition as well as at the top of the Jura member. Sutton Island, Blunts Point, Pettegrove Point, and Jura contain the most outlier high H values. The number of outlier high H points likely contributes to the higher H means observed for the Vera Rubin ridge members of Pettegrove Point (2.2 ± 1.5 wt.% H₂O) and Jura (2.9 ± 2.3 wt.% H₂O).

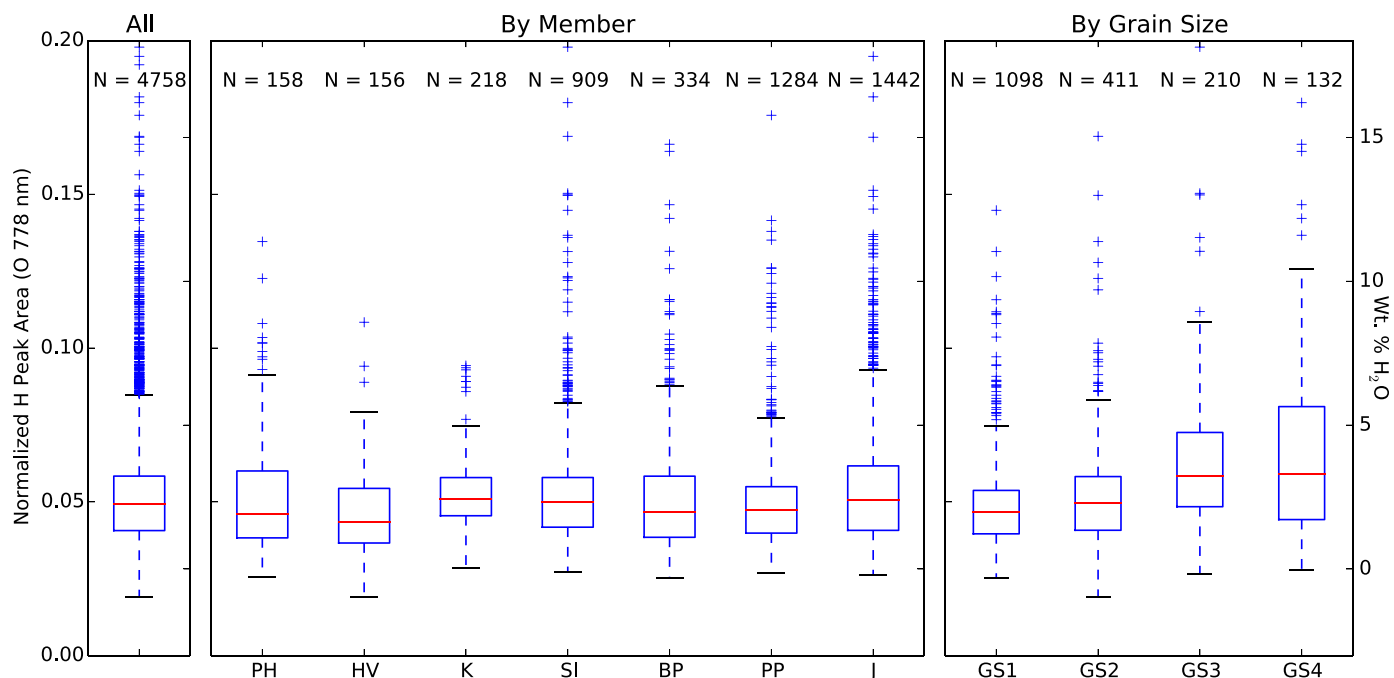


Figure 2. Boxplots showing the distribution of normalized H peak areas for (a) all Murray formation bedrock measurements, (b) each member of the Murray formation, and (c) each Gini index mean score categorized grain size class. The members are Pahrump Hills (PH), Hartmann's Valley (HV), Karasburg (K), Sutton Island (SI), Blunts Point (BP), Pettigrove Point (PP), and Jura (J). The grain size classes are coarse silt and smaller (GS1), coarse silt to very fine sand (GS2), very fine to medium sand (GS3), and medium to very coarse sand (GS4). The box extends from the lower to upper quartile values of the data, with a line at the median. The whiskers extend from the box to show the range of the data. Outlier points are defined as above or below 1.5 times the interquartile range from the median.

The ChemCam H signal distribution varies (~1 wt.%) for bedrock of varying grain sizes as measured by the Gini index mean score (Figure 2; Table 2). Rocks with the finest grains (GS1 category) have a median normalized H peak area of 0.047 or 2.0 wt.% H₂O, whereas rocks with the coarsest grains (GS4 category) have a median normalized H peak area of 0.059 or 3.3 wt.% H₂O. Rocks with coarser grains (spanning the GS3 and GS4 categories) also have larger variance in normalized H peak area, skewed to high H values. Because of the smaller number of rock targets measured in these larger grain size categories, there is not a significant statistical difference between them (Table 2).

4.2. Chemistry of High Hydrogen Content Outliers

The majority of bedrock points targeted by ChemCam have major oxide compositions within the standard compositional range of the Murray formation (Frydenvang et al., 2020; Figure 3). Where chemical composition varies to higher SiO₂, MgO, FeO_T, and CaO, higher normalized H peak areas are sometimes observed. (The apparent H and TiO₂ correlation for SiO₂-rich targets is suspect due to potential ChemCam TiO₂ calibration issues at high Ti; Frydenvang et al., 2017.) We also tested for covariation between ChemCam H signal and major oxide composition for high H (>1 sigma) targets using Principal Components Analysis (PCA; Figure 4). PCA was performed using Python's scikit learn default decomposition package. The first two principal components show a strong covariation between H and MgO and weaker covariation between H and FeO_T. There is also a weak covariation between H and CaO in the first two principal components as well as a potential correlation between H and SiO₂ in the third principal component. There is no correlation; rather, there is an anticorrelation between H and Al₂O₃, Na₂O, and K₂O.

Table 1
T-test on Murray Fm. Members

| | PH | HV | K | SI | BP | PP | J |
|----|--------------|-----------------|-----------------|-----------------|-----------------|-----------------|---|
| PH | 0.006 | 0.460 | 0.445 | 0.453 | 0.129 | 0.053 | |
| HV | | 1.12E-06 | 2.85E-07 | 3.30E-05 | 1.55E-02 | 4.48E-11 | |
| K | | | 0.942 | 0.888 | 8.60E-06 | 0.035 | |
| SI | | | | 0.882 | 1.14E-07 | 0.016 | |
| BP | | | | | 1.69E-03 | 0.179 | |
| PP | | | | | | 1.11E-16 | |
| J | | | | | | | |

Note. A Welch's t test was used to determine if there is a significant difference between the means of the normalized H peak areas for the different members of the Murray formation. Pahrump Hills (PH), Hartmann's Valley (HV), Karasburg (K), Sutton Island (SI), Blunts Point (BP), Pettigrove Point (PP), and Jura (J). Two-tailed *p* values (testing the alternative hypothesis that $\mu_A \neq \mu_B$) are reported; *p* values passing 95% confidence are bolded.

Table 2
T-test on Grain Size Categories

| | GS1 | GS2 | GS3 | GS4 |
|-----|-----|-----------------|-----------------|-----------------|
| GS1 | | 2.91E-05 | 4.44E-16 | 3.38E-11 |
| GS2 | | | 8.06E-09 | 2.43E-07 |
| GS3 | | | | 0.2203 |
| GS4 | | | | |

Note. A Welch's t test was used to determine if there is a significant difference between the means of the normalized H peak areas for the different grain size categories. Coarse silt or smaller (GS1), coarse silt to very fine sand (GS2), very fine to medium sand (GS3), and medium to very coarse sand (GS4). Two-tailed *p* values (testing the alternative hypothesis that $\mu_A \neq \mu_B$) are reported; *p* values passing 95% confidence are bolded.

pore-filling cement (Newsom et al., 2017; Rapin et al., 2016; Rapin et al., 2019). Bedrock targets such as Spectacle Island (Figure 5d), showing no point-to-point physical heterogeneities, can have CaO enrichments up to ~30 wt.% CaO. On average, CaO-enriched targets (>10 wt.% CaO) do not have highly enriched H (average normalized H peak area 0.06; 3.3 wt.% H₂O). A few Ca-sulfate cemented targets, such as Spectacle Island, have higher H up to ~10 wt.% H₂O, but most Ca-sulfate cemented targets have H signals similar to typical bedrock (Figure 3). Some of the highest Ca/high H points occur near the Sutton Island/Blunts Point contact and in the Vera Rubin ridge members (Pettegrove Point, Jura).

Murray formation bedrock targets with high MgO are observed in the Sutton Island member at the transition with the Blunts Point member (Figure 1). ChemCam measurements of these targets show both high MgO (up to 19 wt.% MgO) and high H (normalized H peak area on average 0.11; 8.8 wt.% H₂O). Complementary ChemCam studies have identified S in some of these targets, indicative of hydrated Mg sulfates (Rapin et al., 2019). These Mg- and H-enriched observation points are most commonly observed in planar exposures of eroded bedrock (Figure 5b). In addition to the hydrated Mg sulfates, Mg enrichments occur in planar sandstones (Figure 5c) at the Sutton Island/Blunts Point transition in the Newport Ledge region associated with enriched FeO_T (Figure 1), Mn, and P (Gasda et al., 2018; Gasda et al., 2019; Lanza et al., 2019; Meslin et al., 2018). H is also enriched in these Mg-Fe-Mn-P-enriched targets on average at 0.09 normalized H peak area or 6.5 wt.% H₂O.

At the highest elevation Vera Rubin ridge drill location in the Jura member, Rock Hall, both the target-averaged H signal increased (Figure 1), and the number of elevated H points increased. The bedrock also had a greater roughness at Rock Hall (Figure 5e), potentially contributing to the increased H signal. Associated with elevated H at Rock Hall, ChemCam measured enriched FeO_T (Figure 1), and Cl was observed sporadically in a few observation points near the detection limit (~3 wt.% Cl; Thomas et al., 2019; David et al., 2020). H- and CaO-rich targets are common in this area with occasional Si-rich targets (Figure 1). PCA analysis of high-H targets in the Rock Hall region shows H is most strongly correlated with FeO_T but also associated with CaO (Figure 6).

5. Discussion

5.1. Uncertainties and Causes of Variability

While our initial image classification of ChemCam targets was conducted to remove points with H content potentially impacted by strange surface geometries (cracks, pits, etc.), over 19,000 points were individually classified by eye, and some scatter in the observed point-to-point H signal is likely due to roughness effects missed by the visual classification. H signals averaged by target are likely less influenced by these roughness effects, which might impact 1–2 random points, so overall H trends and median values for each target are more trustworthy than individual point observations and median, and IQR ranges for members are basically unaffected. One possible exception to note is that all targets measured at the Rock Hall locality (within the Jura member) have comparatively rough surfaces at LIBS scale, which may enhance the H signal for that locality.

A number of Murray formation bedrock observations at the base of the Murray formation in the Pahrump Hills member, such as Wallace_ccam (Figure 5a), contain high SiO₂ (up to 70 wt.% SiO₂) (Figure 1). These targets are located at the stratigraphic contact between the Murray formation and the overlying Stimson formation in the Marias Pass region. The high SiO₂ (>60 wt.% SiO₂) targets contain on average 3.5 wt.% H₂O, or 0.06 normalized H peak area, and have grain sizes ranging from silt to medium sand (Rivera-Hernández et al., 2020).

The most frequently enriched major oxide in Murray formation bedrock is CaO (Figure 3). CaO- and H-rich points are scattered throughout the Murray in all members (Figure 1). We excluded Ca-sulfate veins, predominately bassanite in composition according to ChemCam observations (e.g., Rapin et al., 2016), but CaO can also be present in rocks as

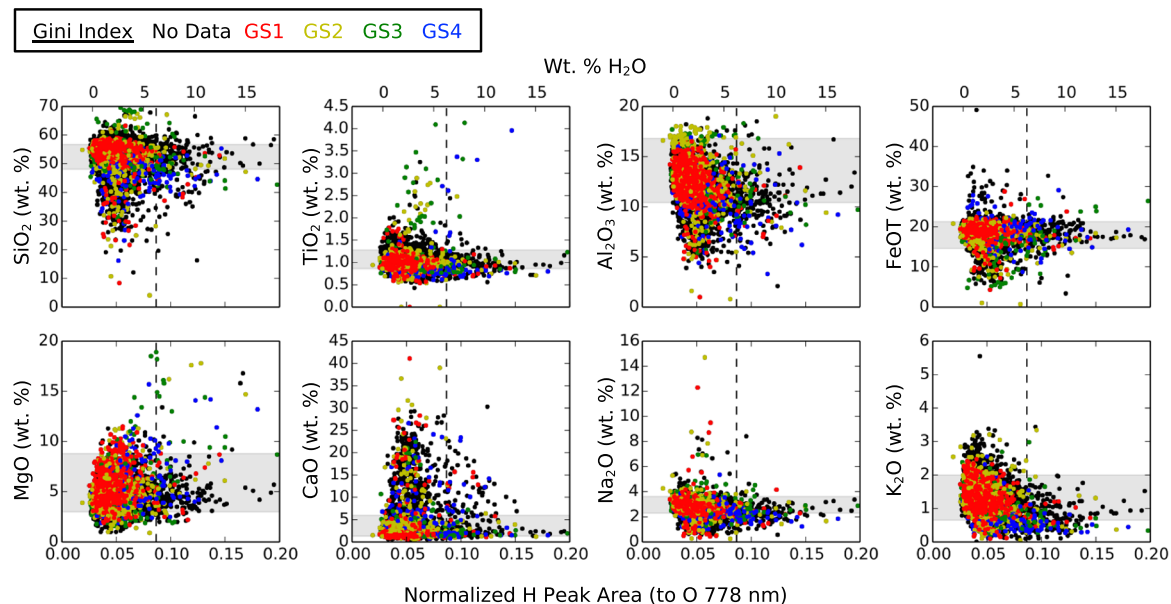


Figure 3. Normalized H peak area, or wt.% H₂O, versus ChemCam major oxides for all Murray formation bedrock observation points. Colors indicate grain size as estimated by the Gini index mean score when available. Vertical dashed line signifies 3-sigma high H outliers. Shaded regions are typical Murray bedrock compositions (Frydenvang, 2020).

While the Gini index mean score only provides an estimate of bedrock grain size (see discussion in section 2), the test for correlation between LIBS H signal and grain size from the Gini index mean score yields only a weak correlation ($R^2 = 0.23$), but the distributions of different grain size categories differ by ~1 wt.% H₂O (Figure 2; Table 2). Future laboratory studies of samples with controlled, varying grain sizes are necessary to quantify how grain size physical matrix effects impact measurement of H and other volatile elements.

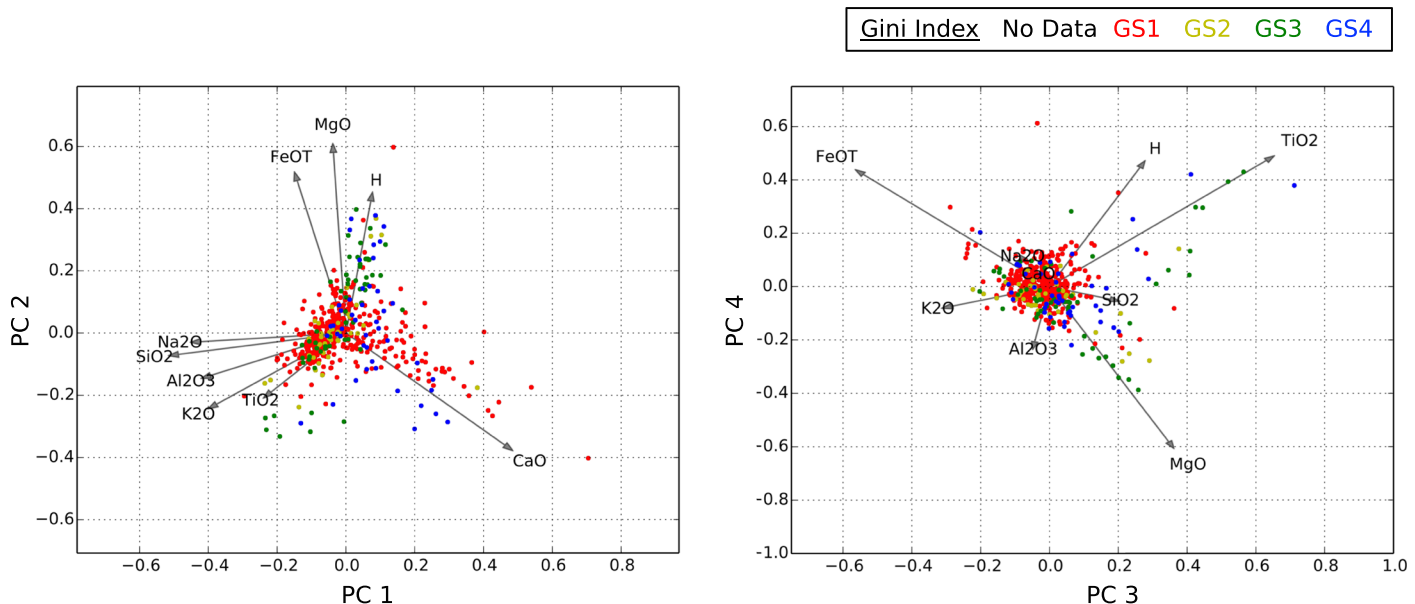


Figure 4. Principal component analysis of Murray formation bedrock observation points containing high H (>1 sigma) chemical composition. Colors indicate grain size as measured by the Gini index mean score. The arrows are the original major oxide and H data axes, projected into the eigenvector space. The arrow lengths represent amount of variance explained by each dimension.

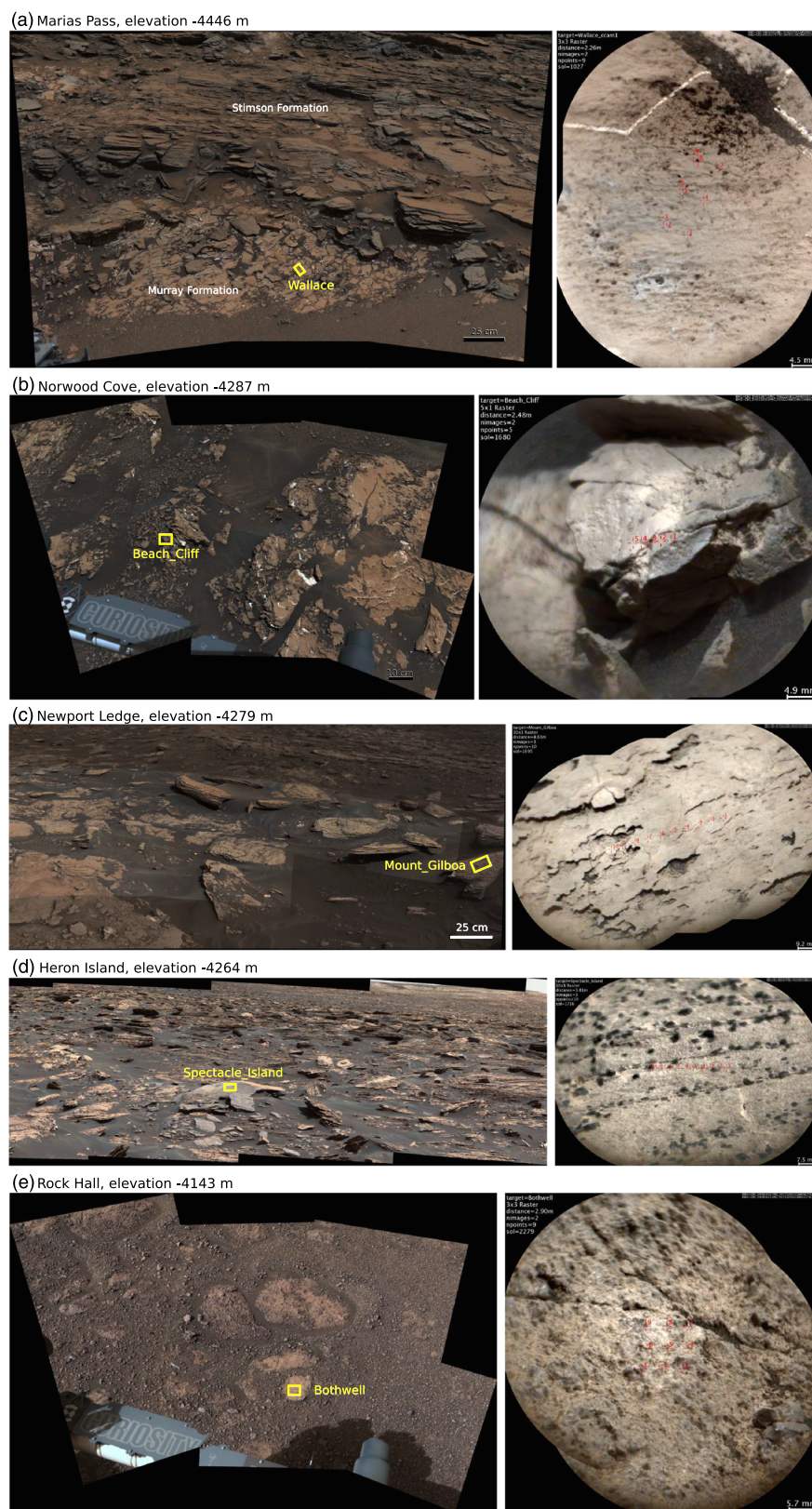


Figure 5. Mastcam mosaics and Remote Micro-Imager images of high normalized H peak area targets: (a) opal measured at Marias Pass, (b) hydrated Mg-sulfates at Norwood Cove, (c) H-rich Mn-oxides at Newport Ledge, (d) hydrated Ca-sulfate cement at Heron Island, and (e) akaganeite at Rock Hall.

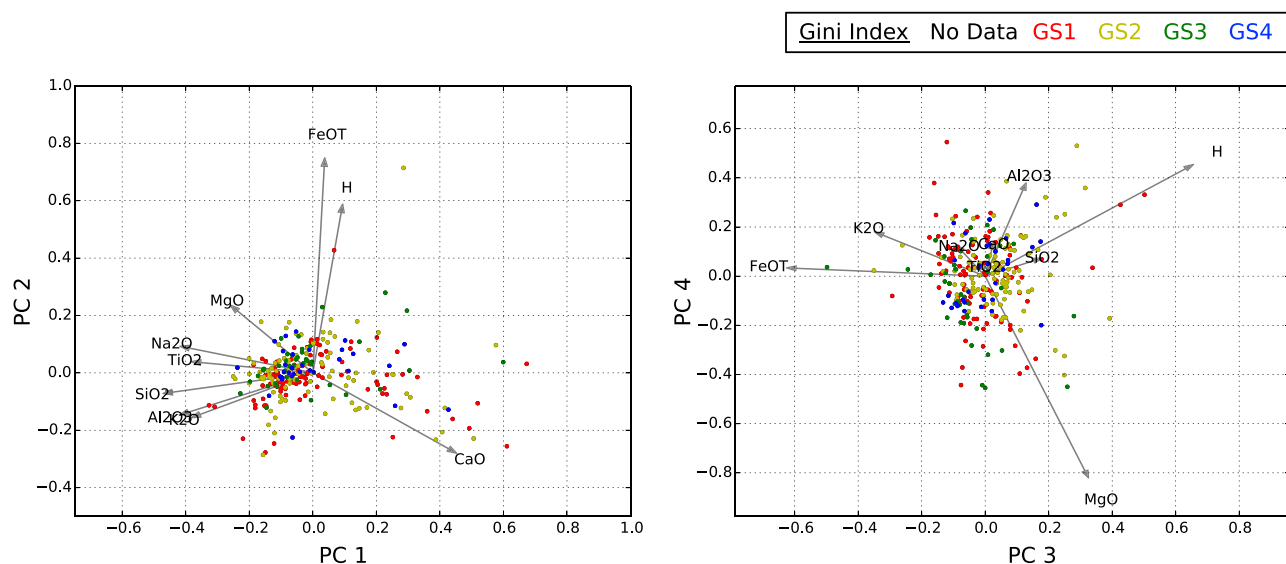


Figure 6. Principal components analysis of Murray formation bedrock observation points containing high H (>1 sigma) chemical composition in the Rock Hall area (elevation greater than $-4,150$ m and less than $-4,140$ m). Colors indicate grain size as measured by the Gini index mean score. The arrows are the original major oxide and H data axes, projected into the eigenvector space. The arrow lengths represent amount of variance explained by each dimension.

5.2. Comparison to Other Instruments

DAN and ChemCam measure different material volumes. ChemCam samples the upper micrometers of the surface over areas ~ 100 s of micrometers whereas DAN is sensitive to geochemistry at depths of ~ 60 cm and across a lateral footprint of ~ 1.5 m in radius (Sanin et al., 2015), so discrepancies between the instruments may be expected depending on the spatial distribution of H reservoirs. The average water content of the Murray formation measured with ChemCam (median: 2.7 wt.% H_2O ; IQR 2.3–3.1 wt.% H_2O) is consistent with measurements by DAN. From sol 753–1292 of the mission, passive DAN experiments of the Murray find on average 1.7 ± 0.7 wt.% H_2O (Tate et al., 2019) and ChemCam measured 2.3 wt.% H_2O on average. DAN has measured 4.2 ± 0.51 wt.% H_2O (Gabriel et al., 2018) at a single bedrock exposure in the upper Murray formation (lower Sutton Island member), where ChemCam measures only 2.1 ± 1.2 wt.% H_2O (target average and standard deviation). Surface dehydration under normal Gale crater environmental conditions (Vaniman et al., 2018) could also explain higher H measured at depth with DAN.

For Murray formation rocks up to the Sutton Island member, the SAM instrument measured at minimum 1.1 ± 0.6 wt.% H_2O at Telegraph Peak and at maximum 2.5 ± 1.6 wt.% H_2O at Mojave (Sutter et al., 2017). Our survey covers the entire Murray formation to Sol 2339 while SAM is limited by drill sampling, making comparison limited to the 10 published drill targets in the Murray formation. ChemCam measurements are similar to this range of values, and SAM estimates may be a lower bound because of loss of some H_2O prior to measurement due to the nature of the preheating ramp to 40 °C (Rapin et al., 2018).

5.3. Carriers of Enrichment

The occurrence of 2.3–3.1 wt.% H_2O in most of the Murray formation bedrock indicates that water is still retained in the present-day dry Martian environment, even just micrometers below the surface. ChemCam cannot measure mineralogy, so we are limited to inferences based on chemical composition and comparison to CheMin for drilled targets. Up to ~ 28 wt.% clay minerals have been detected in Murray formation drilled targets (Bristow et al., 2018). Phyllosilicate interlayer water (the lower temperature 100–300 °C release observed by SAM) and bound OH (the higher temperature 650–800 °C release observed by SAM) (Sutter et al., 2017) likely contribute to ChemCam measured H throughout in the Murray formation. Collapsed smectites under Martian conditions contain 2–7 wt.% H_2O (Bish et al., 2003), consistent with our ChemCam measurement of water content in the Murray. Jarosite, another H-bearing mineral, has been detected by CheMin in Confidence Hills, Mojave, and Telegraph Peak targets (up to ~ 3 wt%; Rampe et al., 2017). In addition, CheMin has measured X-ray amorphous phases in all drilled samples. Phases

such as poorly crystalline aluminosilicate or amorphous silicate (opal-A) and nanophase oxyhydroxides (e.g., ferrihydrite) could contribute to our measured bulk H (Sutter et al., 2017). Here, we discuss potential carriers of enrichment for the ChemCam observed variability in H signal in stratigraphic order.

MSL *Curiosity* observed the contact between the Murray and Stimson formations at Marias Pass. In this region, clear alteration halos were observed crosscutting the unconformity at the Murray/Stimson contact (Frydenvang et al., 2017; Yen et al., 2017). The diagenetic halos are very SiO₂ rich (up to ~90 wt.% SiO₂) and contain elevated H consistent with opal (Rapin et al., 2018). Nearby Murray bedrock targets that are part of our survey are also silica and H enriched (Figure 5a). The opal likely formed from multiple diagenetic fluid events and possibly represents extensive late water-rock interaction (Frydenvang et al., 2017; Rapin et al., 2018). Leaching of Mg, Al, Mn, Fe, Ni, and Zn along with enrichment of Si and S was reported and is consistent with infiltration of subsurface fluids, initially acidic and later alkaline, propagating along fractures crosscutting the Stimson/Murray contact (Yen et al., 2017). The enrichment of Si and H even in visibly unaltered nearby bedrock observed by this study supports pervasive aqueous alteration in the area (Frydenvang et al., 2017). Elevated SiO₂ and H in combination are concentrated in this stratum.

The transition from Sutton Island, composed of heterolithic mudstones and sandstones and interpreted as forming in a marginal lake setting, to Blunts Point, primarily finely laminated mudstones interpreted as forming in a suspension/fall-out lacustrine setting (Fedo et al., 2018), has both elevated bulk (target-averaged) H and outlier high H targets. On the Norwood Cove target, high H is associated with elevated Mg. Rapin et al. (2019) have reported high S in these Mg- and H-enriched targets relative to surrounding bedrock occurring in a relatively thin (<10 m) stratigraphic interval within cm-thick planar exposures of erosion-resistant rocks. Early diagenetic precipitation from a concentrated, saline brine created by evaporation is the favored formation pathway for these hydrated Mg sulfates (Rapin et al., 2019).

Starting in the Karasburg member, the Murray formation is also often variably enriched in Ca sulfate mixed in the bedrock (Rapin et al., 2019). While this bedrock Ca-sulfate cement is typically not enriched in H according to our measurements, a few targets such as Spectacle_Island have higher H more consistent with bassanite (6.21 wt.% H₂O) than anhydrite. Our observations of varying H signals in Ca-sulfate enriched targets are consistent with CheMin measurements of gypsum, bassanite, and anhydrite occurring together in Gale sedimentary rocks (Vaniman et al., 2018). The observed frequency of hydrated Ca-sulfate cements in the Murray implies extensive S-rich groundwater crystallization and, in some cases, can correspond to primary deposition (Rapin et al., 2019).

The Newport Ledge area is also at the transition from the Sutton Island to Blunts Point member. Newport Ledge sandstones have on average 4.6 wt.% MnO_T in dark-toned rocks and 1.5 wt.% MnO_T in light-toned rocks compared to 0.5 wt.% MnO_T on average in Sutton Island and Blunts Point (Gasda et al., 2019). Previously, ChemCam observed high MnO_T targets in Yellowknife Bay and the Kimberly formation where the oxides may have been deposited by past groundwaters (Lanza et al., 2016). In the Murray, FeO_T and MgO are enriched with MnO_T in some targets (Figure 1). These targets, such as Mount_Gilboa (Figure 5c), are H enriched and contain on average 6.6 ± 3.8 wt.% H₂O. Variable P is detected in Newport Ledge targets (Meslin et al., 2018). The most likely carrier phase is hydrous Mn oxides and Fe oxides with adsorbed phosphates (Meslin et al., 2018). Hydrous Mn oxides and Fe oxides suggest oxidizing, aqueous conditions either during primary sediment deposition within the lake and/or in groundwaters post lithification (Lanza et al., 2019; Meslin et al., 2018). The deposits at Newport Ledge may be due to changes in water depth or shifting shoreline locations (Lanza et al., 2019).

At the Rock Hall drill site, at the top of the Vera Rubin ridge in the Jura member, ChemCam observations indicate a substantial increase in bedrock H content (5.5 ± 3.4 wt.% H₂O). Some of this increase may be related to the roughness effect; targets at Rock Hall appear rougher (on the ~mm to cm scale) than typical Murray bedrock (Figure 5). ChemCam observes enriched FeO_T correlated with higher H at Rock Hall (Figure 1). CheMin has detected ~7 wt.% akageneite, a chlorine bearing iron hydroxide, and ~1 wt.% jarosite, an Fe-containing sulfate hydroxide (Morris et al., 2019). This CheMin analysis along with our observed FeO_T/H correlation suggests akageneite and jarosite may be among the H carrier phases. Rock Hall is quite different from other Vera Rubin ridge drill targets; akageneite is present at levels higher than hematite, and more jarosite is present. SAM also observes nitrates and oxychlorine (Rampe et al., 2020), suggesting the Rock Hall area experienced interaction with later saline fluids. While our measurements of H at Rock

Hall are subject to higher uncertainty due to roughness, SAM and CheMin observations confirm Rock Hall is different from other Vera Rubin ridge areas and some of the observed H increase is likely real.

Variability in the average H content of the Murray formation as well as observations of specific H-enriched phases in specific intervals of the Murray formation suggest a history of multiple episodes of water-rock interaction with distinctive fluids. Disentangling changes in lakewater fluid chemistry from later diagenetic fluid events is difficult, but large-scale variation in bedrock H such as enrichment at the Sutton Island/Blunts Point transition may point to changes in the Gale crater paleoenvironment, which produced more saline, oxidized lakewaters that precipitated hydrated sulfates and hydrous Mn oxides. Both the Marias Pass and Rock Hall H variability is likely due to later groundwater episodes of alteration forming diverse H-bearing silica phases (opal) or the oxidative dissolution/precipitation of Fe (II) minerals, respectively.

6. Conclusions

We have quantified the ChemCam normalized H peak area for all Murray formation bedrock targets up to mission Sol 2339 and found the Murray formation contains a median value of 2.7 wt.% H₂O with an IQR of 2.3–3.1 wt.% H₂O. While our measurement uncertainty of H in individual ChemCam observation points is high (approximately ± 2.1 wt.% H₂O), the target-averaged (5–10 points) uncertainty is lower (approximately ± 0.8 wt.% H₂O). Targets were filtered to exclude those with roughness effects that can artificially increase the H signal and its point-to-point variability. We examined the grain size of the Murray formation rocks and found that grain size could exert a ~1 wt.% influence on H signal intensity. Future controlled laboratory studies are required to quantify the dependence of rock grain size on the H signal, and future laboratory studies will measure the dependence of grain size on the H signal.

ChemCam data reveal significant H enrichment in select intervals within the Murray formation that signify distinctive aqueous processes. While the target-averaged H signal remains constant for most of the Murray formation, the Hartmann's Valley shows lower H signal from the other members and also has the lowest clay content measured by CheMin (3 ± 1 wt.%; Bristow et al., 2018). Carriers of H enrichment in the Murray formation include clays, amorphous materials, and Ca sulfates throughout. Enrichment in Si and H at Marias Pass only, indicates opal formed, likely from extensive late-stage alteration at the unconformable Stimson/Murray contact at Marias Pass, after both units had already been deposited. Enrichment in H at the Sutton Island/Blunts Point transition and the presence of hydrated Mg-sulfates and hydrated Ca sulfates in beds and Fe/Mn oxides in bedrock and nodules suggests changing lakewaters including increased salinity and changes in lakewater depth or shoreline location. Akaganeite, jarosite, and other iron-bearing phases are potential carrier phases of the high H observed at Rock Hall at the Vera Rubin Ridge. Si-enriched high H points are also found here, and complementary SAM and CheMin observations suggest Rock Hall bedrock experienced alteration by later saline, oxidative fluids. The stratigraphic control on the variability in the H signal of Murray bedrock thus clearly indicates changes in both the depositional environment and later diagenetic fluid events, in a multistage sequence of aqueous activity at Gale crater.

Acknowledgments

Work at Caltech was supported by a NASA MSL Participating Scientist Program grant to B. L. Ehlmann and a National Science Foundation Graduate Research Fellowship Grant DGE-1144469 to N. H. Thomas. N. H. Thomas thanks the LSSTC Data Science Fellowship Program, which is funded by LSSTC, NSF Cybertraining Grant 1829740, the Brinson Foundation, and the Moore Foundation; her participation in the program has benefited this work. Supporting laboratory data have been previously published in Thomas et al. (2018). ChemCam data used for this paper, including major oxide compositions, are publicly available on the Planetary Data System (<http://pds-geosciences.wustl.edu/missions/msl/chemcam.htm>). Data table containing the measured H (normalized H peak area to O 778 nm) for every ChemCam Murray formation bedrock observation point is publicly available as a Caltech data record (<https://doi.org/10.22002/D1.1349>). Gini index mean scores used in this paper are publicly available at Zenodo (<https://doi.org/10.5281/zenodo.3605603>).

References

- Anderson, R. B., Morris, R. V., Clegg, S. M., Bell, J. F., Wiens, R. C., Humphries, S. D., et al. (2017). The influence of multivariate analysis methods and target grain size on the accuracy of remote quantitative chemical analysis of rocks using laser induced breakdown spectroscopy. *Icarus*, 215(2), 608–627. <http://doi.org/10.1016/j.icarus.2011.07.034>
- Banham, S. G., Gupta, S., Rubin, D. M., Watkins, J. A., Sumner, D. Y., Edgett, K. S., et al. (2018). Ancient Martian aeolian processes and palaeomorphology reconstructed from the Stimson formation on the lower slope of Aeolis Mons, Gale crater, Mars. *Sedimentology*, 65(4). <https://doi.org/10.1111/sed.12469>
- Bish, D. L., Carey, W., Vaniman, D. T., & Chipera, S. J. (2003). Stability of hydrous minerals on the Martian surface. *Icarus*, 164(1), 96–103. [http://doi.org/10.1016/S0019-1035\(03\)00140-4](http://doi.org/10.1016/S0019-1035(03)00140-4)
- Blake, D., Vaniman, D., Achilles, C., Anderson, R., Bish, D., Bristow, T., et al. (2012). Characterization and calibration of the CheMin mineralogical instrument on Mars Science Laboratory. *Space Science Reviews*, 170(1–4), 341–399. <http://doi.org/10.1007/s11214-012-9905-1>
- Bristow, T. F., Rampe, E. B., Achilles, C. N., Blake, D. F., Chipera, S. J., Craig, P., et al. (2018). Clay mineral diversity and abundance in sedimentary rocks of Gale crater, Mars. *Science Advances*, 4(6), eaar3330. <http://doi.org/10.1126/sciadv.aar3330>
- Clegg, S. M., Wiens, R. C., Anderson, R., Forni, O., Frydenvang, J., Lasue, J., et al. (2017). Recalibration of the Mars Science Laboratory ChemCam instrument with an expanded geochemical database. *Spectrochimica Acta Part B: Atomic Spectroscopy*, 129, 64–85. <https://doi.org/10.1016/j.sab.2016.12.003>
- David, G., Cousin, A., Forni, O., Meslin, P.-Y., Dehouck, E., Mangold, J., et al. (2020). Analyses of high-iron sedimentary bedrock and diagenetic features observed with ChemCam at Vera Rubin ridge, Gale crater, Mars: calibration and characterization. *Journal of Geophysical Research: Planets*. <https://doi.org/10.1029/2019JE006314>

- Edgar, L. A., Fedo, C. M., Gupta, S., Banham, S. G., Fraeman, A. A., Grotzinger, J. P., et al. (2020). A lacustrine paleoenvironment recorded at Vera Rubin ridge, Gale crater: Overview of the sedimentology and stratigraphy observed by the Mars Science Laboratory Curiosity rover. *Journal of Geophysical Research: Planets*, 125, e2019JE006307. <https://doi.org/10.1029/2019JE006307>
- Fedo, C. M., Grotzinger, J. P., Gupta, S., Fraeman, A. A., Edgar, L., Edgett, K., et al. (2018). Sedimentology and stratigraphy of the Murray formation, Gale Crater, Mars. Paper presented at 49th Lunar and Planetary Science Conference, The Woodlands, TX (p. 2083).
- Fraeman, A. A., Arvidson, R. E., Catalano, J. G., Grotzinger, J. P., Morris, R. V., Murchie, S. L., et al. (2013). A hematite-bearing layer in Gale Crater, Mars: Mapping and implications for past aqueous conditions. *Geology*, 41(10), 1103–1106. <https://doi.org/10.1130/G34613.1>
- Fraeman, A. A., Ehlmann, B. L., Arvidson, R. E., Edwards, C. S., Grotzinger, J. P., Milliken, R. E., et al. (2016). The stratigraphy and evolution of lower Mount Sharp from spectral, morphological, and thermophysical orbital data sets. *Journal of Geophysical Research: Planets*, 121, 1713–1736. <http://doi.org/10.1002/2016JE005095>
- Fraeman, A. A., Johnson, J. R., Arvidson, R. E., Rice, M. S., Wellington, D. F., Morris, R. V., et al. (2020). Synergistic ground and orbital observations of iron oxides on Mt. Sharp and Vera Rubin ridge. *Journal of Geophysical Research: Planets*, 125, e2019JE006294. <https://doi.org/10.1029/2019JE006294>
- Frydenvang, J., Mangold, N., Wiens, R., Fraeman, A. A., Edgar, L. A., Fedo, C., et al. (2020). The chemostratigraphy of the Murray Formation and role of diagenesis at Vera Rubin Ridge in Gale Crater, Mars, as observed by the ChemCam instrument. *Journal of Geophysical Research: Planets*, 125, e2019JE006320. <https://doi.org/10.1029/2019JE006320>
- Frydenvang, J., Gasda, P. J., Hurowitz, J. A., Grotzinger, J. P., Wiens, R. C., Newsom, H. E., et al. (2017). Diagenetic silica enrichment and late-stage groundwater activity in Gale crater, Mars. *Geophysical Research Letters*, 44, 4716–4724. <http://doi.org/10.1002/2017GL073323>
- Gabriel, T. S. J., Hardgrove, C., Czarnecki, S., Rampe, E. B., Rapin, W., Achilles, C. N., et al. (2018). Water abundance of dunes in Gale Crater, Mars from active neutron experiments and implications for amorphous phases. *Geophysical Research Letters*, 45, 12,766–12,775. <http://doi.org/10.1029/2018GL079045>
- Gasda, P. J., Lanza, N. L., Lamm, S. N., L'Haridon, J., Meslin, P.-Y., Forni, O., et al. (2018). Evidence of redox sensitive elements associated with possible shoreline deposits in Gale Crater. Paper presented at 49th lunar and planetary Science conference, the woodlands, TX (p. 2483).
- Gasda, P. J., Lanza, N. L., Meslin, P.-Y., Forni, O., L'Haridon, J., Fischer, W. W., et al. (2019). High-Mn sandstone as evidence for oxidized conditions in Gale Crater Lake. Paper presented at 50th Lunar and Planetary Science Conference, The Woodlands, TX (p. 1620).
- Grotzinger, J. P., Gupta, S., Malin, M. C., Rubin, D. M., Schieber, J., Siebach, K., et al. (2015). Deposition, exhumation, and paleoclimate of an ancient lake deposit, Gale crater, Mars. 350(6257), aac7575. <http://doi.org/10.1126/science.aac7575>
- Grotzinger, J. P., Sumner, D. Y., Kah, L. C., Stack, K., Gupta, S., Edgar, L., et al., & MSL Science Team (2014). A habitable fluvio-lacustrine environment at Yellowknife Bay, Gale crater, Mars. *Science*, 343(6169). <https://doi.org/10.1126/science.1242777>
- Gwizd, S., Fedo, C., Grotzinger, J., Edgett, K., Rivera-Hernández, F., Stein, N. (2019). Depositional history of the Hartmann's valley member, Murray formation, Gale crater, Mars. *LPSC 49*. Abstract 2150.
- Hurowitz, J. A., Grotzinger, J. P., Fischer, W. W., McLennan, S. M., Milliken, R. E., Stein, N., et al. (2017). Redox stratification of an ancient lake in Gale Crater, Mars. *Science*, 356(6341), eaah6849. <http://doi.org/10.1126/science.eah6849>
- Lanza, N. L., Fischer, W. W., Lamm, S. N., Gasda, P. J., Meslin, P.-Y., Ollila, A. M., et al. (2019). Variable redox conditions in Gale Crater as indicated by manganese abundance along the curiosity traverse. Paper presented at 50th Lunar and Planetary Science Conference, The Woodlands, TX (p. 3146).
- Lanza, N. L., Wiens, R. C., Arvidson, R. E., Clark, B. C., Fischer, W. W., Gellert, R., ... Zorzano, M.-P. (2016). Oxidation of manganese in an ancient aquifer, Kimberley formation, Gale crater Mars. *Geophysical Research Letters*, 43, 7398–7407. <https://doi.org/10.1002/2016gl069109>
- Mahaffy, P. R., Webster, C. R., Cabane, M., Conrad, P. G., Coll, P., Atreya, S. K., et al. (2012). The sample analysis at Mars investigation and instrument suite. *Space Science Reviews*, 170(1–4), 401–478. <http://doi.org/10.1007/s11214-012-9879-z>
- Mangold, N., Dehouck, E., Fedo, C., Forni, O., Achilles, C., Bristow, T., et al. (2019). Chemical alteration of fine-grained sedimentary rocks at Gale crater. *Icarus*, 321(March 2018), 619–631. <http://doi.org/10.1016/j.icarus.2018.11.004>
- Maurice, S., Wiens, R. C., Saccoccia, M., Barraclough, B., Gasnault, O., Forni, O., et al. (2012). The ChemCam instrument suite on the Mars Science Laboratory (MSL) Rover: Science objectives and mast unit description. *Space Science Reviews*, 170(1–4), 95–166. <http://doi.org/10.1007/s11214-012-9912-2>
- Meslin, P.-Y., Gasda, P., L'Haridon, J., Forni, O., Lanza, N., Lamm, S., et al. (2018). Detection of hydrous manganese and Iron oxides with variable phosphorous and magnesium contents in the lacustrine sediments of the Murray formation, Gale, Mars. Paper presented at 49th Lunar and Planetary Science Conference, The Woodlands, TX (p. 1447).
- Meslin, P.-Y., Gasnault, O., Forni, O., Schröder, S., Cousin, A., Berger, G., et al., & MSL Science Team Science (2013). Soil diversity and hydration as observed by ChemCam at Gale Crater, Mars. *Science*, 341(6153), 1238670. <http://doi.org/10.1126/science.1238670>
- Milliken, R. E., Grotzinger, J. P., & Thomson, B. J. (2010). Paleoclimate of Mars as captured by the stratigraphic record in Gale crater. *Geophysical Research Letters*, 37, L04201. <http://doi.org/10.1029/2009GL041870>
- Mitrofanov, I. G., Litvak, M. L., Varenikov, A. B., Barmakov, Y. N., Behar, A., Bobrovitsky, Y. I., et al. (2012). Dynamic Albedo of Neutrons (DAN) experiment onboard NASA's Mars Science Laboratory. *Space Science Reviews*, 170(1–4), 559–582. <http://doi.org/10.1007/s11214-012-9924-y>
- Morris, R. V., Bristow, T. F., Rampe, E. B., Yen, A. S., Vaniman, D. T., Tu, V., et al. (2019). Mineralogy and formation processes for the Vera Rubin Ridge at Gale Crater, Mars from CheMin XRD analyses. Paper presented at 50th Lunar and Planetary Science Conference, The Woodlands, TX (p. 1127).
- Nachon, M., Clegg, S. M., Mangold, N., Schröder, S., Kah, L. C., Dromart, G., et al. (2014). Calcium sulfate veins characterized by ChemCam/curiosity at Gale crater, Mars. *Journal of Geophysical Research, Planets*, 119, 1991–2016. <http://doi.org/10.1002/2013JE004588>
- Newsom, H. E., Jackson, R., Wiens, R. C., Frydenvang, J., Gasda, P., Lanza, N., et al. (2017). Increasing occurrences of sandstone cemented with calcium sulfate on Mount Sharp, Gale Crater, Mars. Paper presented at 48th Lunar and Planetary Science Conference, The Woodlands, TX (p. 2495).
- Rampe, E. B., Ming, D. W., Blake, D. F., Bristow, T. F., Chipera, S. J., Grotzinger, J. P., et al. (2017). Mineralogy of an ancient lacustrine mudstone succession from the Murray formation, Gale crater, Mars. *Earth and Planetary Science Letters*, 471, 172–185. <http://doi.org/10.1016/j.epsl.2017.04.021>
- Rampe, E. B., Bristow, T. F., Morris, R. V., Morrison, S. M., Achilles, C. N., Ming, D. W., et al. (2020). Mineralogy of Vera Rubin ridge from the Mars Science Laboratory CheMin instrument. *Journal of Geophysical Research: Planets*, 125, e2019JE006306. <https://doi.org/10.1029/2019JE006306>

- Rapin W. (2016). Hydratation de la surface de Mars à partir des données du rover Curiosity, PhD Thesis, Université Paul Sabatier (Toulouse III).
- Rapin, W., Bousquet, B., Lasue, J., Meslin, P.-Y., Lacour, J.-L., Fabre, C., et al. (2017). Roughness effects on the hydrogen signal in laser-induced breakdown spectroscopy. *Spectrochimica Acta Part B: Atomic Spectroscopy*, 137, 13–22. <http://doi.org/10.1016/j.sab.2017.09.003>
- Rapin, W., Chauviré, B., Gabriel, T. S. J., McAdam, A. C., Ehlmann, B. L., Hardgrove, C., et al. (2018). In situ analysis of opal in Gale Crater, Mars. *Journal of Geophysical Research, Planets*, 123(8), 1955–1972. <http://doi.org/10.1029/2017JE005483>
- Rapin, W., Ehlmann, B. L., Dromart, G., Schieber, J., Thomas, N., Fischer, W. W., et al. (2019). High salinity recorded by bedrock Sulfate enrichments at Gale Crater. Paper presented at 50th Lunar and Planetary Science Conference, The Woodlands, TX (p. 2147).
- Rapin, W., Meslin, P.-Y., Maurice, S., Vaniman, D., Nachon, M., Mangold, N., et al. (2016). Hydration state of calcium sulfates in Gale crater, Mars: Identification of bassanite veins. *Earth and Planetary Science Letters*, 452, 197–205. <http://doi.org/10.1016/j.epsl.2016.07.045>
- Rapin, W., Meslin, P.-Y., Maurice, S., Wiens, R. C., Laporte, D., Chauviré, B., et al. (2017). Quantification of water content by laser induced breakdown spectroscopy on Mars. *Spectrochimica Acta Part B: Atomic Spectroscopy*, 130, 82–100. <http://doi.org/10.1016/j.sab.2017.02.007>
- Rivera-Hernández, F., Sumner, D. Y., Mangold, N., Banham, S. G., Edgett, K. S., Fedo, C. M., et al. (2020). Grain size variations in the Murray formation: Stratigraphic evidence for changing depositional environments in Gale Crater, Mars. *Journal of Geophysical Research, Planets*, 125. <https://doi.org/10.1029/2019JE006230>
- Rivera-Hernández, F., Sumner, D. Y., Mangold, N., Stack, K. M., Forni, O., Newsom, H., et al. (2019). Using ChemCam LIBS data to constrain grain size in rocks on Mars: Proof of concept and application to rocks at Yellowknife Bay and Pahrump Hills, Gale crater. *Icarus*, 321, 82–98. <http://doi.org/10.1016/j.icarus.2018.10.023>
- Sanin, A. B., Mitrofanov, I. G., Litvak, M. L., Lisov, D. I., Starr, R., Boynton, W., et al. (2015). Data processing of the active neutron experiment DAN for a Martian regolith investigation. *Nuclear Instruments and Methods in Physics Research Section A: Accelerators, Spectrometers, Detectors and Associated Equipment*, 789, 114–127. <http://doi.org/10.1016/j.nima.2015.03.085>
- Schröder, S., Meslin, P.-Y., Gasnault, O., Maurice, S., Cousin, A., Wiens, R. C., et al. (2015). Hydrogen detection with ChemCam at Gale Crater. *Icarus*, 249, 43–61. <http://doi.org/10.1016/j.icarus.2014.08.029>
- Schröder, S., Rammelkamp, K., Vogt, D. S., Gasnault, O., & Hübers, H.-W. (2019). Contribution of a Martian atmosphere to laser-induced breakdown spectroscopy (LIBS) data and testing its emission characteristics for normalization applications (2019). *Icarus*, 325, 1–15. <http://doi.org/10.1016/j.icarus.2019.02.017>
- Stack, K. M., Sun, V. Z., Arvidson, R. E., Fedo, C., Day, M., Bennett, K., et al. (2019). Origin of linear ridges in the clay-bearing unit of Mount Sharp, Gale Crater, Mars. *LPSC 50*. Abstract 1210.
- Stein, N., Grotzinger, J. P., Schieber, J., Mangold, N., Hallet, B., Newsom, H., et al. (2018). Desiccation cracks provide evidence of lake drying on Mars, Sutton Island member, Murray formation, Gale Crater. *Geology*, 46(6), 515–518. <https://doi.org/10.1130/G40005.1>
- Sutter, B., McAdam, A. C., Mahaffy, P. R., Ming, D. W., Edgett, K. S., Rampe, E. B., et al. (2017). Evolved gas analyses of sedimentary rocks and eolian sediment in Gale Crater, Mars: Results of the Curiosity rover's sample analysis at Mars instrument from Yellowknife Bay to the Namib Dune. *Journal of Geophysical Research, Planets*, 122, 2574–2609. <http://doi.org/10.1002/2016JE005225>
- Tate, C. G., Moersch, J. E., Mitrofanov, I., Litvak, M., Bellutta, P., Boynton, W. V., et al. (2019). Mars Science Laboratory dynamic albedo of neutrons passive mode data and results from Sols 753 to 1292: Pahrump Hills to Naukluft Plateau. Paper presented in 50th lunar and planetary Science conference, the woodlands, TX (p. 2132).
- Thomas, N. H., Ehlmann, B. L., Anderson, D. E., Clegg, S. M., Forni, O., Schröder, S., et al. (2018). Characterization of hydrogen in basaltic materials with laser-induced breakdown spectroscopy (LIBS) for application to MSL ChemCam data. *Journal of Geophysical Research, Planets*, 123, 1996–2021. <http://doi.org/10.1029/2017JE005467>
- Thomas, N. H., Ehlmann, B. L., Meslin, P. -Y., Rapin, W., Anderson, D. E., Rivera-Hernández, F., et al. (2019). Mars Science Laboratory observations of chloride salts in Gale Crater, Mars. *Geophysical Research Letters*, 46, 10754–10763. <https://doi.org/10.1029/2019GL082764>
- Vaniman, D. T., Martinez, G. M., Rampe, E. B., Bristow, T. F., Blake, D. F., Yen, A. S., et al. (2018). Gypsum, bassanite, and anhydrite at Gale crater, Mars. *American Mineralogist*, 103(7), 1011–1020. <http://doi.org/10.2138/am-2018-6346>
- Wiens, R. C., Maurice, S., Barracough, B., Saccoccia, M., Barkley, W. C., Bell, J. F., et al. (2012). The ChemCam instrument suite on the Mars Science Laboratory (MSL) rover: Body unit and combined system tests. *Space Science Reviews*, 170(1–4), 167–227. <http://doi.org/10.1007/s11214-012-9902-4>
- Wiens, R. C., Maurice, S., Lasue, J., Forni, O., Anderson, R. B., Clegg, S., et al., & the ChemCam team (2013). Pre-flight calibration and initial data processing for the ChemCam laser-induced breakdown spectroscopy instrument on the Mars Science laboratory rover. *Spectrochimica Acta B*, 82, 1–27. <http://doi.org/10.1016/j.sab.2013.02.003>
- Williams, R. M. E., Grotzinger, J. P., Dietrich, W. E., Gupta, S., Sumner, D. Y., Wiens, R. C., et al. (2013). Martians fluvial conglomerates at Gale Crater. *Science*, 340(6136), 1068–1072. <https://doi.org/10.1126/science.1237317>
- Yen, A. S., Ming, D. W., Vaniman, D. T., Gellert, R., Blake, D. F., Morris, R. V., et al. (2017). Multiple stages of aqueous alteration along fractures in mudstone and sandstone strata in Gale Crater, Mars. *Earth and Planetary Science Letters*, 471, 186–198. <https://doi.org/10.1016/j.epsl.2017.04.033>
- Ytsma, C. R., & Dyar, M. D. (2018). Effects of univariate and multivariate regression on the accuracy of hydrogen quantification with laser-induced breakdown spectroscopy. *Spectrochimica Acta B*, 139, 27–37. <http://doi.org/10.1016/j.sab.2017.11.010>